Supercontinuum generation in ZBLAN fibers—detailed comparison between measurement and simulation

Agger, Christian; Petersen, Christian ; Dupont, Sune ; Steffensen, Henrik; Lyngsø, Jens Kristian; Thomsen, Carsten L.; Thøgersen, Jan; Keiding, Søren Rud; Bang, Ole

Published in:
Optical Society of America. Journal B: Optical Physics

Publication date:
2012

Supercontinuum generation in ZBLAN fibers—detailed comparison between measurement and simulation

Christian Agger,[3] Christian Petersen,[1] Sune Dupont,[1] Henrik Steffensen,[3] Jens Kristian Lyngsø,[2] Carsten L. Thomsen,[2] Jan Thøgersen,[1] Søren R. Keiding,[1] and Ole Bang[3,*]

[1]*DTU Fotonik, Department of Photonics Engineering, Technical University of Denmark, 2800 Kongens Lyngby, Denmark*
[2]*Department of Chemistry, Aarhus University, Langelandsgade 140, 8000 Aarhus C, Denmark*
[3]*NKT Photonics A/S, Blokken 84, 3460 Birkerød, Denmark*
**Corresponding author: oban@fotonik.dtu.dk*

Received September 30, 2011; revised December 10, 2011; accepted December 12, 2011;
posted December 14, 2011 (Doc. ID 155765); published March 16, 2012

We present a detailed comparison between modeling and experiments on supercontinuum (SC) generation in a commercial ZBLAN step-index fiber. Special emphasis is put on identifying accurate material parameters by incorporating measurements of the ZBLAN Raman gain, fiber dispersion, and loss. This identification of accurate parameters is of great importance to substantiate numerical simulations of SC generation in soft-glass fibers. Good agreement between measurement and simulation is obtained when pumping both in the normal and anomalous dispersion regimes. © 2012 Optical Society of America

OCIS codes: 190.4370, 190.5650.

1. INTRODUCTION

Supercontinuum (SC) light has been a topic of much research interest since it was first observed in bulk material by Alfano and Shapiro in 1970 [1]. Since then, the field of supercontinuum generation (SCG) in optical fibers based on fused silica has developed rapidly and SC has found applications in, e.g., confocal microscopy, coherent anti-Stokes Raman spectroscopy [2], and optical coherence tomography [3]. A review of the physics of SCG in photonic crystal fibers based on fused silica glass is given in [4]. A key contribution to the successful generation of optical SC sources has been the existing detailed knowledge about the optical properties of silica, allowing accurate numerical modeling. The ability to model SCG in silica-based fibers has been a great benefit for developing commercial SC sources [5].

Fused silica, however, becomes highly absorbing above 2.5 μm, and thus it cannot be used if one wants to extend the long wavelength edge of SC light beyond this limit. Soft glasses, such as tellurite (TeO_2—Na_2O—ZnF_2), chalcogenide (typically As_2Se_3), or ZBLAN (ZrF_4—BaF_2—LaF_3—AlF_3—NaF), are promising in this respect, because these materials all can have high transmissions in the near- and mid-infrared (mid-IR) ranges [6]. Furthermore, ZBLAN has a nonlinear refractive index comparable to silica [7–10], whereas tellurite and in particular chalcogenide have substantially stronger nonlinear properties [6,11–16].

IR SC has applications in IR microscopes [17], pollution monitoring, countermeasures, green chemistry, and optical components testing, and SC spectra from soft-glass fibers with bandwidths ranging from approximately 1 to 4.5 μm and as far as 6.5 μm have been reported [8,18–19]. These reports have presented both experimentally achieved results and, with varying success, spectra calculated numerically based on the generalized nonlinear Schrödinger equation (GNLSE). Soft glasses though, are much less well documented materials than fused silica and furthermore, as they are composite materials, their optical properties vary between structural compositions. Therefore, it is hard to determine material parameters that are accurate enough to allow reliable numerical calculations. Thus, in simulations of SCG in soft-glass fibers, it is often seen that the Raman response of fused silica is used or that no Raman response is cited or shown, even though it has been included. Similarly the material dispersion and attenuation used in a given simulation are often not reported or mentioned only briefly.

Because most soft glasses have material zero dispersion wavelengths (ZDWs) at longer wavelengths than fused silica, some newly proposed IR SC sources, which focus on commercial Yb or Er pump lasers, are based on cascading a silica fiber with a soft-glass fiber [18–19]. The SC is then initially generated in the silica fiber and then coupled into a soft-glass fiber that pushes the SC further into the IR. However, such coupling between nonlinear fibers for improved redshift of solitons into the IR pose requirements on the matching of the dispersion and nonlinear properties of the fibers [20–21].

In this work, we present a detailed comparison of modeling and experiments for SCG in a commercially available step-index ZBLAN fiber [FiberLabs, 03B-2-3(09C-27)]. We experimentally obtain material parameters, based on which the numerical model can predict measured SCG, both when pumping in the normal and anomalous dispersion regime. The measured material parameters include the dispersion, attenuation, and Raman response of the fiber. As mentioned, the Raman response of ZBLAN, in particular, is a source of uncertainty in reported numerical simulations of SCG. Based on a pulsed Raman measurement in the actual fiber we investigate here [22], we find a value of $f_R = 0.062$ of the fractional Raman contribution in our ZBLAN fiber. The reason why our value differs significantly from the values of $f_R = 0.193$ given in [9], the value of $f_R = 0.20$ chosen in [10], and the value of $f_R = 0.24$

found in [23], is discussed in Subsection 4.C. The wavelength dependence of the fiber attenuation is also of great importance, and for SCG in tellurite it has been shown that the length of fiber used should be optimized to achieve the broadest spectrum, or fiber attenuation may otherwise reduce the SC spectral bandwidth [16,24]. In ZBLAN, ultrabroadband spectra stretching up to 6.28 μm have also been demonstrated, by using short lengths of fiber, thus reducing the effect of confinement loss [8].

The paper is organized as follows: in Section 2 the experimental setup for SC measurements is presented, in Section 3 we present the numerical model used for simulating SCG, and in Section 4 we discuss the dispersion profile, attenuation, and Raman response function used in SCG simulations. The Raman response function is based on our measurement of the Raman gain in ZBLAN presented in [22]. Finally, in Section 5, we compare measurements and simulations of SCG.

2. EXPERIMENTAL SETUP FOR SCG MEASUREMENTS

The main laser system, shown in Fig. 1, consists of a Ti:sapphire regenerative amplifier, which gives 800 nm pulses with a FWHM of 100 fs and a pulse energy of 1 mJ. We use the output to pump a tunable optical parametric amplifier system (TOPAS, Light Conversion) thereby generating the pump pulse for the SC. The use of a TOPAS allows us to tune the pump wavelength in the range from 1200 to 2600 nm. We are thus able to pump the fiber both above and below the ZDW. The pulse energy of the pump is controlled by filters. Usually, the output from the TOPAS is strongly attenuated, yielding pulse energies on the order of 1 μJ. The pulse duration of the pump is determined by an intensity dependent autocorrelation, and the pump is coupled into the ZBLAN fiber with an efficiency around 30% using a ×10 focusing objective. The output from the fiber is collimated using a gold off-axis parabolic reflector with a focal length of 25 mm. The use of reflective optics ensures that the output from the fiber is not influenced by chromatic aberrations. The collimated output is sent to a scanning monochromator (Spectrapro 2300i, Acton Research). The light is focused at the entry slit of the monochromator by a CaF_2 lens with a focal length of 15 cm. The dispersed light at the exit slit is detected using a two-color detector (Si/PbSe, Hamamatsu) connected to a boxcar integrator synchronized with the laser system. Appropriate filters are inserted to suppress higher order diffraction artifacts. The spectrum is finally compiled from measurements with the various filters and gratings, as well as measurements with both Si and PbSe detectors to cover the entire wavelength range from the visible to the mid-IR. A correction is performed to account for the wavelength dependent efficiency of detectors and gratings. The output spectral density is normalized to the measured total output power.

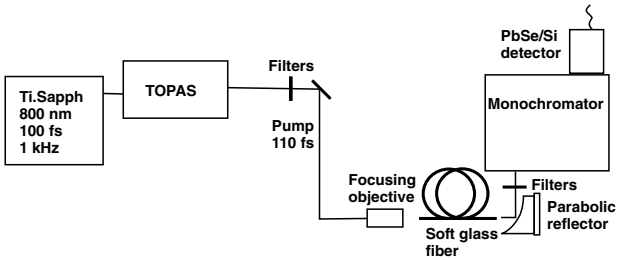

Fig. 1. Experimental setup for our SC measurement.

3. NUMERICAL MODEL

To model SCG in soft-glass optical fibers, we solve the GNLSE to obtain the electric field envelope $A = A(z,T)$ as a function of the longitudinal position z in a retarded time frame T moving with the group velocity $v_g = 1/\beta_1(\omega_p)$ at the pump frequency ω_p, where $\beta_1 = \beta_1(\omega) = d\beta/d\omega$ and $\beta = \beta(\omega)$ is the mode propagation constant. The electric field envelope A is related to the instantaneous power by $P = P(z,T) = |A|^2$ with physical units of watts (W). Consequently, by Parceval's theorem, $|\tilde{A}|^2$ has units of Js and represents the energy spectral density (ESD) in the frequency domain, where $\tilde{A} = \tilde{A}(z,\omega)$ is the Fourier transform of A. In our simulations we have used a chirp-free Gaussian-shaped pump pulse of the form,

$$A(0,T) = \sqrt{P_0}e^{-\frac{T^2}{2T_0^2}} + \text{OPPM}, \tag{1}$$

as the initial condition, where the pulse shape, peak power P_0, and pulse width $T_0 = T_{\text{FWHM}}/(2\sqrt{\ln 2})$ are determined from autocorrelation of the input pulse, as described in Section 2. The last term in Eq. (1) represents the one-photon-per-mode (OPPM) noise model that is used to model spectral fluctuations from shot to shot in the input pulse [4,25]. The input pulse has a central carrier wavelength $\lambda_p = 2\pi c/\omega_p$, where c is the speed of light in vacuum.

The GNLSE has previously shown its applicability in modeling SCG in silica fibers [4]. In this work, we solve a version of the GNLSE, based on a derivation by Lægsgaard [26], which accurately includes the frequency dependence of the effective area. We solve the GNLSE in the frequency domain in the interaction picture introduced by Hult [27]. It can be shown that the GNLSE can then be written as [25]

$$\frac{\partial \tilde{C}_I}{\partial z} = i\gamma\frac{\omega}{\omega_0}e^{\tilde{\tilde{L}}z}\mathcal{F}\{C\mathcal{F}^{-1}\{\tilde{R}\mathcal{F}\{|C|^2\}\}\}, \tag{2}$$

where $\tilde{\tilde{L}} = \tilde{\tilde{L}}(\omega)$ is a linear operator; ω_0 is the calculation expansion frequency, which is generally different from ω_p; and $\mathcal{F}\{\cdot\}$ denotes the Fourier transform. Here $C = C(z,T)$ is a pseudo electric field envelope with Fourier transform $\tilde{C} = \tilde{C}(z,\omega)$, and $\tilde{C}_I = \tilde{C}_I(z,\omega)$ is then $\tilde{C}$ transformed into the interaction picture as follows:

$$\tilde{C}_I = e^{-\tilde{\tilde{L}}z}\tilde{C} \quad \text{and} \quad \tilde{C}\left[\frac{A_{\text{eff}}}{A_{\text{eff}}(\omega_0)}\right]^{\frac{1}{4}} = \tilde{A}, \tag{3}$$

where $A_{eff} = A_{eff}(\omega)$ is the effective area of the fiber mode. The linear operator $\tilde{\tilde{L}}$ in Eq. (2) is given by

$$\tilde{\tilde{L}} = i(\beta - \beta(\omega_0) - \beta_1(\omega_p)[\omega - \omega_0]) - \frac{\alpha}{2}, \tag{4}$$

where $\alpha = \alpha(\omega)$ is the power attenuation in the fiber. Notice that the retarded time frame T moves with the group velocity v_g at the pump frequency. This is why ω_p appears in Eq. (4) and, as mentioned earlier, generally $\omega_0 \neq \omega_p$, in order to allow the calculation domain to extend to wavelengths below half the pump wavelength. In the version of the GNLSE used here, the nonlinear coefficient is

$$\gamma = \gamma(\omega) = \frac{\omega_0 n_2 n_{\text{eff}}(\omega_0)}{c n_{\text{eff}} \sqrt{A_{\text{eff}} A_{\text{eff}}(\omega_0)}}, \tag{5}$$

where $n_2 = 2.1 \cdot 10^{-20}$ m^2/W is the generally accepted value of the nonlinear refractive index of ZBLAN [7–10] and $n_{\text{eff}} = n_{\text{eff}}(\omega)$ is the effective index of the fundamental mode. The function $\tilde{R} = \tilde{R}(\Omega)$ in Eq. (2) is the Fourier transform of the Raman response function, and $\Omega = \omega - \omega_0$.

In all simulations presented below, Eq. (2) is solved using a fourth-order Runge–Kutta integration scheme [28] with adaptive step size, where the error is controlled by the local goal-error method [29]. It can be shown [30] that if loss is neglected and the waveguide maintains its dispersion properties along its length (i.e., no fiber taper, etc.), the interaction picture GNLSE (2) conserves the photon number

$$P_N(z) \equiv \frac{c\sqrt{A_{\text{eff}}(\omega_0)}}{n_2 n_{\text{eff}}(\omega_0)} \int_{-\infty}^{\infty} n_{\text{eff}} \sqrt{A_{\text{eff}}} \frac{|\tilde{C}_I|^2}{\omega} \mathrm{d}\omega \tag{6}$$

during propagation; i.e., $dP_N(z)/dz = 0$. The conservation of this quantity is used to check the implementation of Eq. (2) in a simulation where loss is ignored. The conservation is quantified through the photon number error $\text{Err}(z) \equiv |P_N(z) - P_N(0)|/P_N(0)$.

A. Interpreting Results from Simulations

The results of our simulations are depicted in terms of the ESD in the wavelength domain, given by

$$\text{ESD}(z, \lambda) = \frac{c}{\lambda^2} |\tilde{A}(z, \lambda)|^2, \tag{7}$$

which corresponds to the power spectral density (PSD), $\text{PSD} = f_{\text{rep}}\text{ESD}$, where f_{rep} is the seed laser repetition rate.

When noise fluctuations on the input pulse are included in the calculations, it is necessary to perform an ensemble average over multiple independent simulations with different noise seeds [4,25]. Using Eq. (7), the ensemble averaged PSD is given by

$$\text{PSD} = \frac{c f_{\text{rep}}}{\lambda^2} \langle |\tilde{A}(z, \lambda)|^2 \rangle, \tag{8}$$

where the angle brackets denote the averaging over N independent simulations. This averaging procedure corresponds to the finite integration time of the boxcar integrator, mentioned in Section 2, that records the SC PSD in the experiments [4]. In our setup, the seed laser has a repetition rate of $f_{\text{rep}} = 1$ kHz and the integration time of the boxcar is set to $\tau_{\text{int}} = 300$ ms. Thus, each experimentally recorded spectrum is averaged over $N_r = 300$ shots from the seed laser, and ideally each simulated SC spectrum should contain an equal amount of shots in the ensemble average.

The spectrometer described in Section 2, has a finite wavelength resolution and reports all light in a wavelength region of width $\Delta\lambda_{\text{res}}$ as being at one discrete wavelength. Because several gratings are used during measurement of such wide SC spectra as reported here, this wavelength resolution differs slightly between measurements in the different regimes. When reporting simulation results, we take the wavelength resolution to be $\Delta\lambda_{\text{res}} = 10$ nm and perform a running average using a rectangular box of width $\Delta\lambda_{\text{res}}$.

4. ACCURATE MATERIAL PARAMETERS

We consider a commercially available ZBLAN step-index fiber from FiberLabs with a core composition of (53%ZrF_4—29%BaF_2—3%LaF_3—3%AlF_3—12%NaF). The particular fiber has a $d = 10.7$ μm core diameter, and a numerical aperture of NA $= (n_{co}^2 - n_{cl}^2)^{1/2} = 0.2$, where n_{co} (n_{cl}) is the core (cladding) refractive index [31]. The NA is to a good approximation independent of frequency according to the fiber manufacturer [31]. The fiber is calculated to be multimoded below 2.8 μm, and experimentally we do observe signs that not just the fundamental mode is present in the output spectrum at short wavelengths. Special care is taken to match the numerical apertures of coupling lenses and the fiber, in order to minimize the coupling to higher order modes. In our simulations, we make the typical assumption [4] that all light propagates in the fundamental mode of the fiber during SCG, which can cause some discrepancy between measurement and simulation in the short wavelength regime.

A. Fiber Dispersion

Knowledge of the group-velocity dispersion (GVD) $\beta_2 = \beta_2(\omega) = d^2\beta/d\omega^2$, and in particular the location of the ZDW is of paramount importance for the characteristics of any kind of SCG process [4,32–33].

In this work, the GVD profile is found numerically using a commercial finite element tool, the fiber geometry reported by the fiber manufacturer, and a Sellmeier fit of the ZBLAN material dispersion from the literature [34]. The calculated GVD parameter is transformed to the fiber dispersion $D(\lambda) \equiv -2\pi c\beta_2/\lambda^2$ and shown as the solid black curve in Fig. 2.

Because ZBLAN is a composite glass, material dispersion can vary between manufacturers and also between production batches. Using variations of the Sellmeier fit when predicting the fiber dispersion properties will cause uncertainty in, for example, the location of the ZDW. To mitigate any influence of possible discrepancies between the literature material dispersion and the actual fiber material dispersion, we measured the dispersion profile of the fiber. The measurement was made using an interferometric procedure [35] but, due to spectrometer limitations, in a smaller wavelength region than the one of total interest for SCG. The measured dispersion profile is shown in solid red in Fig. 2. The dispersion

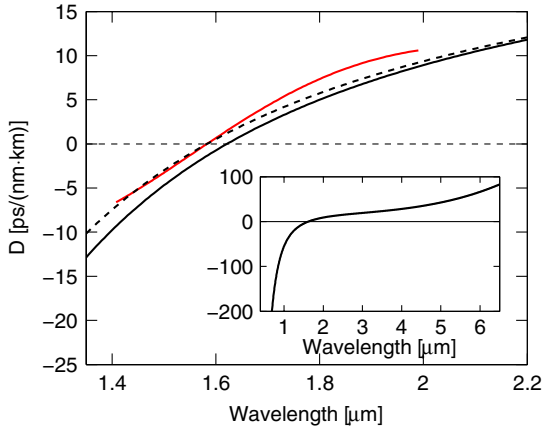

Fig. 2. (Color online) Dispersion parameters: solid black curve, calculated dispersion parameter; red curve, measured dispersion profile; dashed black, dispersion calculated from wavelength-shifted effective index (inset, dispersion in the full calculation domain).

measurement has some degree of uncertainty because the fiber is multimoded below 2.8 μm. This uncertainty, along with the possible discrepancy between the fiber material and the literature reported refractive index wavelength dependence, is manifested in Fig. 2. Here it is shown that the calculated ZDW is $\lambda_{\mathrm{ZD}}^{c} = 1.62$ μm, while the measured is $\lambda_{\mathrm{ZD}}^{m} = 1.58$ μm. We seek to address this difference of $\lambda_s = \lambda_{\mathrm{ZD}}^{c} - \lambda_{\mathrm{ZD}}^{m} = 40$ nm by also considering a second dispersion profile, found by shifting the calculated profile, such as to have a ZDW that coincides with the measured. This is achieved by defining a wavelength-shifted propagation constant $\beta' = \beta'(\omega) = \omega n'_{\mathrm{eff}}(\omega)/c$, where $n'_{\mathrm{eff}} = n_{\mathrm{eff}}(\lambda + \lambda_s)$ is the corresponding wavelength-shifted effective refractive index. We use both the calculated propagation constant and the wavelength-shifted propagation constant in simulations so as to investigate the influence of ZDW discrepancies. The dispersion profile calculated from the wavelength-shifted effective refractive index is displayed as the black dashed curve in Fig. 2.

B. Fiber Attenuation

A measurement of the total fiber attenuation $\alpha = \alpha(\omega)$ is provided by FiberLabs and is shown in the black, lower curve in Fig. 3(a) [31]. This loss curve is measured soon after the fiber drawing but for a different yet similar fiber as the one we investigate here. The loss data between 700 and 3200 nm were measured by the cutback method for a multimode ZBLAN fiber. The values for wavelengths longer than 3.2 μm and shorter than 700 nm were estimated values [31]. The measurement resolution was 20 nm, but some degree of uncertainty is to be expected according to the manufacturer [31]. Based on deviations between experiment and simulations presented in Section 5, we suspect that an attenuation band starting around 2.7 μm is present in experiments, and this is not accounted for by the measured loss curve in Fig. 3(a). We also suspect that such an attenuation band can be due to water (OH) intruding the fiber, because water is known to cause absorption peaks in this particular wavelength range in fluoride-based fibers [36–37]. Furthermore, we note that water vapor present in the air also has absorption lines in this region of the spectrum.

To examine this, we have added an artificial loss peak to the measured loss. We have investigated both Gaussian- and parabolic-shaped additions of different peak values, and widths, and redone simulations. We found that a parabolic-shaped loss [shown in blue in Fig. 3(a)] with a peak value of 5 dB/m, coinciding with the small peak of the experimental loss curve, i.e., centered at 2.9 μm, will give simulation results (shown in blue in Figs. 8 and 10) that substantiate the long wavelength edge trends exhibited by our measured PSDs.

C. Raman Response

In the frequency domain, the Raman response function is written as [38]

$$\tilde{R} = (1 - f_R) + f_R \mathcal{F}\{h_R(T)\}, \tag{9}$$

where the first term accounts for the instantaneous response of the material, $h_R(T)$ is the delayed Raman response in the time domain derived from the Raman gain spectrum, and f_R is the fractional Raman contribution. From a given Raman gain profile $g_R = g_R(\Omega)$, the time response function $h_R(T)$ is calculated as [38–39]

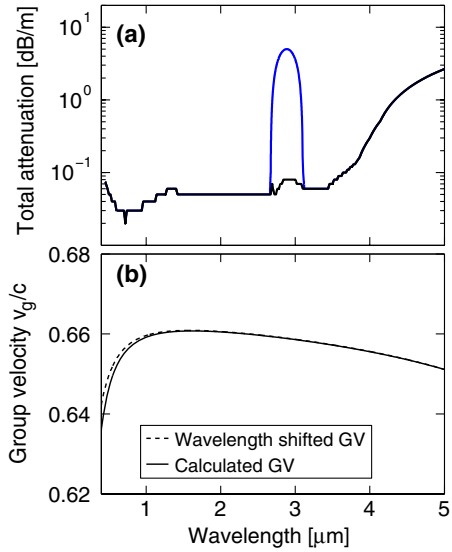

Fig. 3. (Color online) (a) Black, lower, solid curve is measured absorption in a multimode fiber (courtesy FiberLabs [31]), and the blue, upper curve is the artificially added loss due to OH. (b) GV curves from both $\beta(\omega)$ and $\beta'(\omega)$.

$$h_R(T) = \frac{\theta(T)}{f_R} \frac{c}{\pi n_2 \omega_p^R} \int_0^\infty g_R(\Omega) \sin(\Omega T) \mathrm{d}\Omega, \tag{10}$$

where $\theta(T)$ is the Heaviside step function that ensures causality; ω_p^R is the frequency of the pump pulse, at $\lambda_p^R = 1650$ nm, used in the gain profile measurement experiment; and f_R is found as a normalization factor by requiring that $\int_{-\infty}^{\infty} h_R(T)\mathrm{d}T = 1$.

To establish the functional form, described by Eq. (9) of the Raman response in ZBLAN, we have measured the Raman gain profile in our fiber [22]. The measurement was performed in a copropagating pump–probe experiment, and the recorded gain profile is shown in Fig. 4. As in the earlier mentioned studies [40–42], we also find that the ZBLAN gain spectrum has a prominent and narrow gain band located at $\nu_1 = 17.4$ THz Stokes shift and a broader gain band around $\nu_2 = 12.4$ THz. In the copropagating pump–probe experiment, it is not possible to measure the gain spectrum for small Stokes shifts due to a strong background contribution from the pump. However, measurements of the spontaneous Raman scattering spectrum for ZBLAN display nonvanishing values of the scattering cross section for low Stokes shifts [43]. To accommodate this nonvanishing gain for small Stokes shifts, the measured Raman gain is fitted to a sum of two Gaussian functions, so the gain profile takes the form

$$g_R(\Omega) = a_1 e^{-\frac{(\Omega/(2\pi)-\nu_1)^2}{2w_1^2}} + a_2 e^{-\frac{(\Omega/(2\pi)-\nu_2)^2}{2w_2^2}}. \tag{11}$$

The Gaussian fit is shown in solid black in Fig. 4, and the coefficients for Eq. (11) are listed in Table 1. From the measured gain profile and Eq. (10), we find $f_R = 0.062$.

Let us relate our measured Raman gain spectrum with existing literature: the Raman response in bulk samples of binary compositions of fluorozirconate glass (ZrF_4—BaF_2) was analyzed in 1981 in [40], and a strong Raman gain was identified between 17.0 and 17.9 THz, depending on the content of ZrF_4 in the glass (52–74%). In 1985 a ZBLAN fiber with a core

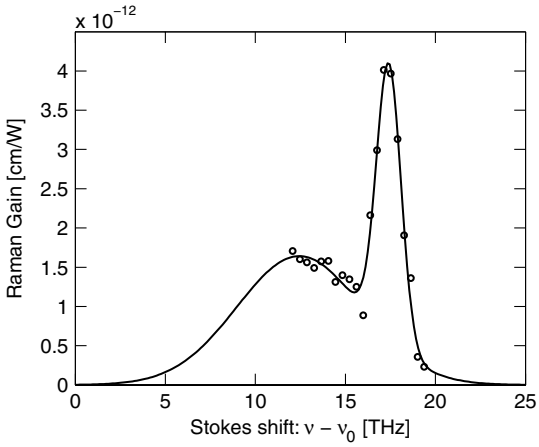

Fig. 4. Raman gain profile measured at $\lambda_p^R = 2\pi c/\omega_p^R = 1650$ nm. Dots are experimental data, and the solid curve shows the fit given by Eq. (11) and Table 1 [22].

diameter of 18–30 μm (from Le Verre Fluoré) was measured to have a peak Raman gain of $a_1 = 1 - 3 \cdot 10^{-11}$ cm/W at a Stokes shift of $\nu_1 = 17.7$ THz when pumping at 1.0 μm [41]. Also in 1985, a ZBLAN fiber with a core diameter of 65 μm (60%ZrF_4—30%BaF_2—3%LaF_3—4%AlF_3—3%NaF) was measured at 514.5 nm to have a Raman peak at $\nu_1 = 17.4$ THz with a maximum gain of $6 \cdot 10^{-11}$ cm/W [43]. A smaller peak Raman gain of $a_1 = (2 \pm 0.5) \cdot 10^{-11}$ cm/W at a Stokes shift of $\nu_1 = 17.9$ THz was measured at 580 nm in a ZBLAN fiber with core diameter of 70 μm (from Le Verre Fluoré) in 1993 [42]. Here a second broader local maximum gain was also observed at a Stokes shift of $\nu_2 = 10.2$ THz [42].

In 2011 the full Raman gain spectrum was measured at 1650 nm in a ZBLAN fiber (53%ZrF_4—29%BaF_2—3%LaF_3—3%AlF_3—12%NaF) with a core diameter of 10.7 μm by us, as detailed above [22]. Our measurements confirm the ZBLAN peak at $\nu_1 = 17.4$ THz, and we also find a second broader peak as in [42] but at $\nu_2 = 12.4$ THz. Recently, bulk measurements of a ZBLAN glass with the same composition as the fiber investigated here by us and in [22] placed the two peaks at 17.7 and 8.4 THz with identical amplitudes of $1.15 \cdot 10^{-11}$ cm/W [23].

The parameters for the Raman response of ZBLAN fibers (except [23], which is in bulk), with the amplitudes scaled to a measurement wavelength of 1060 nm, are summarized in Table 1. All measurements agree in that the main gain peak is around 17.4 THz. In contrast, there is a large spread in the location of the broad gain peak we find at 12.4 THz. The spread in the amplitude of the main gain peak value (a_1) is a factor 7 and thus quite significant. Here it is important to realize that ZBLAN is a composite material with properties that depend on the specific composition. In addition, the process of fiber drawing has a significant influence on the resulting material properties of ZBLAN as, e.g., shown in [44], where it was found that the drawing process reduces the refractive index on the order of 10^{-3}. This could be one reason for the difference between our fiber Raman gain and the bulk Raman gain measured in [23], where both of us use the exact same ZBLAN composition.

For simulations, not only the specific fitting parameters but also the integrated fractional Raman contribution f_R are important. If we again compare with [23], then their value of $f_R = 0.24$, is four times larger than our value. This is, in particular, a result of their low-frequency broad gain peak being much stronger than ours. In fact, the difference could be even larger, taking into account that a nonlinear refractive index of $n_2 = 5.4 \cdot 10^{-20}$ m^2/W is used in [23] and that f_R scales with n_2 as seen in Eq. (10). Here we use the generally accepted value of $n_2 = 2.1 \cdot 10^{-20}$ m^2/W [7–10]. One reason for the discrepancy in the f_R values could again be the influence of fiber drawing [44].

We finally note that a general uncertainty in the value of f_R for ZBLAN is observed in the literature on numerical modeling. For example, f_R is sometimes simply assumed to have a value close to silica, $f_R = 0.2$ [10] or data from the ZBLAN Raman gain (with two main peaks) is inserted into a single oscillator model, e.g., giving $f_R = 0.19$ [9]. In the following, we will use the Raman gain measured by ourselves, because it is for the specific fiber we use.

5. SUPERCONTINUUM GENERATION IN ZBLAN

We consider SCG in the ZBLAN fiber when pumping both in the normal and the anomalous dispersion regime. The initial condition for simulations is given by Eq. (1). In all simulations, the number of points on the frequency/time axis is $N_t = 2^{17}$ and the GNLSE is solved in the wavelength window [0.45;6] μm, which has a corresponding expansion wavelength $\lambda_0 = 2\pi c/\omega_0 = 837.2$ nm. The time resolution is $dt = 1.62$ fs, and the frequency resolution is $d\omega = 2.25 \cdot 10^{15}$ rad/s. The local goal error is $\delta_g = 10^{-6}$, and the fiber length is $L = 1.85$ m. Using these numerical parameters, the calculation time is on the order of a few days for a single shot, and thus to limit the computational effort, we use only $N_c = N_r/10 = 30$ independent runs for each ensemble average in the procedure discussed in Subsection 3.A. To check the numerical implementation of the GNLSE, the photon number error is plotted in Fig. 5, for a typical simulation with $P_0 = 1110$ kW, $T_{\mathrm{FWHM}} = 110$ fs and $\lambda_p = 2000$ nm, corresponding to the simulation shown in Fig. 10, though neglecting loss and noise. Here it is seen that the relative error stays below $5 \cdot 10^{-6}$.

Table 1. Raman Gain Parameters Scaled to a Measurement Wavelength of 1060 nm

Ref.	a_1	a_2	ν_1	ν_2	w_1	w_2	f_R
	[10^{-11} cm/W]		[THz]		[THz]		
[9]	3.6	—	17.7	—	1.19	—	0.19
[22]	0.54	0.25	17.4	12.4	0.68	3.5	0.06
[23]	0.85	0.85	17.7	8.4	2.7	12.9	0.24
[41]	1–3	—	17.7	—	—	—	—
[42]	1.09	—	17.9	10.2	—	—	—
[43]	2.91	—	17.4	—	—	—	—

A. Normal Dispersion Regime Pumping

For pumping in the normal dispersion regime, the seed laser is adjusted to output pulses of width $T_{\mathrm{FWHM}} = 145$ fs at $\lambda_p = 1450$ nm. These parameters are fixed throughout our measurements and simulations in the normal dispersion regime.

In the normal dispersion pumping regime the pulse spectrum should initially broaden symmetrically due to self-phase modulation (SPM), so that light will cross the ZDW into the anomalous dispersion regime. This initial symmetrical spectral buildup is also observed in the spectrograms shown in Figs. 6(a)–6(b). The soliton number

$$N = \sqrt{\frac{n_2\omega_{\mathrm{sol}}}{cA_{\mathrm{eff}}(\omega_{\mathrm{sol}})}\frac{P_0T_0^2}{|\beta_2(\omega_{\mathrm{sol}})|}}, \tag{12}$$

where ω_{sol} is the frequency of the soliton, is not well defined in the normal dispersion regime, but as light passes the ZDW into the anomalous dispersion, N becomes large because $\beta_2 \to 0$ at the ZDW. This means that a significant amount of solitons are generated even though only a fraction of the pump power passes the ZDW by SPM. After a short distance of propagation, these solitons undergo redshift due to soliton self-frequency shift (SSFS) while emitting nonsolitonic radiation (dispersive waves) on the normal dispersion side of the ZDW [45]. At the output of the fiber, at least $N = 6$ solitons, group velocity matched with nonsolitonic radiation [marked by vertical dotted lines in Fig. 6(c)], are clearly distinguishable and normal dispersion regime pumping can thus generate a broad SC,

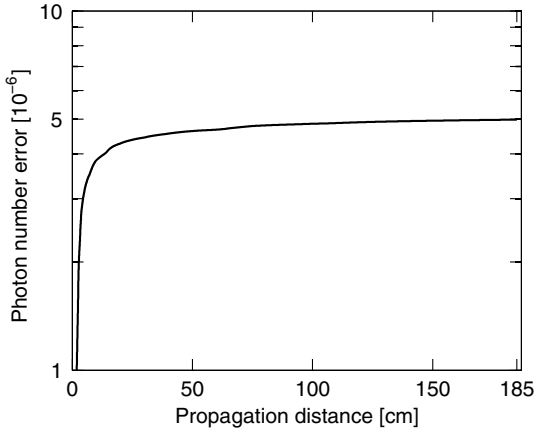

Fig. 5. Photon number error as a function of the propagation distance for a typical simulation neglecting loss and noise. $P_0 = 1110$ kW, $T_{\mathrm{FWHM}} = 110$ fs and $\lambda_p = 2000$ nm.

as was also found recently in [8] in ZBLAN and previously in 1978 in silica [46].

A comparison between measurement (black) and simulations (green) is shown in Fig. 7 for a peak power of $P_0 = 710$ kW and in Figs. 8(a) 8(b) for $P_0 = 1180$ kW. The red curve is calculated using the wavelength-shifted dispersion profile (dashed black in Fig. 2). The dashed vertical lines in Figs. 7 and 8 (and 10 and 11) mark the pump wavelength (black), the calculated ZDW (green), and the wavelength-shifted ZDW (red), respectively.

In Fig. 7 we see a larger level of the calculated PSD at short wavelengths compared to the measured, which gives an

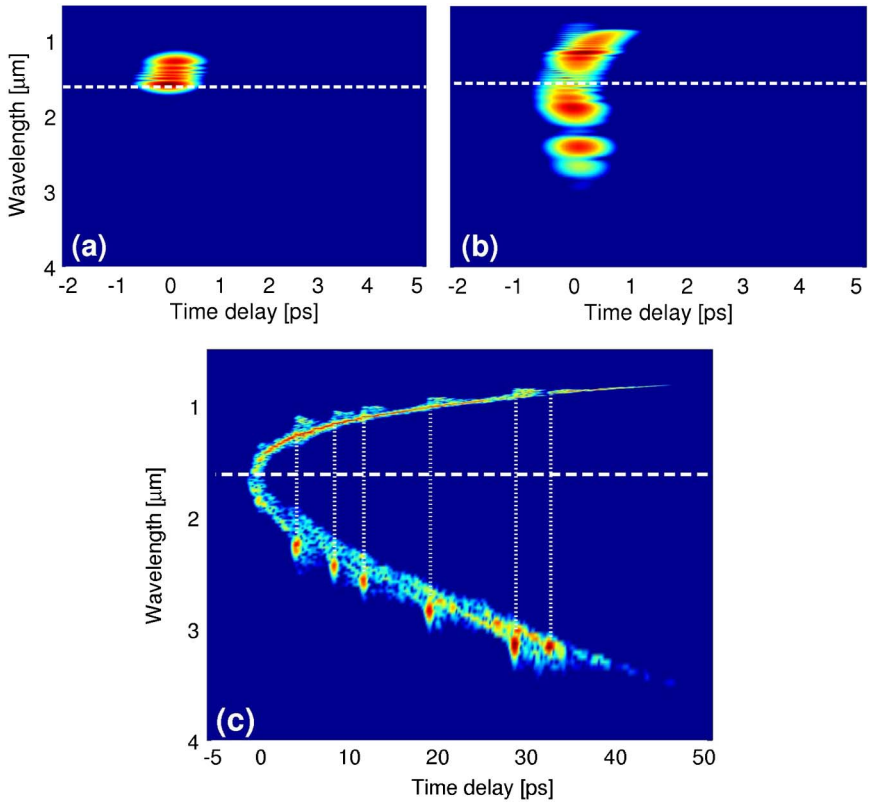

Fig. 6. (Color online) Spectrograms of the $\lambda_p = 1450$ nm and $P_0 = 1180$ kW simulation at (a) $z = 1.0$ cm, (b) $z = 5.3$ cm, and (c) $z = L$. The white dashed line marks the calculated ZDW of the fiber.

indication that the calculated dispersion is not exactly corresponding to the physical dispersion of the fiber. This indication is clear, because it is the abrupt fall-off of the GV at short wavelengths, clearly shown in Fig. 3(b), that determines the location of the short-wavelength edge of the SC [47–48].

One consistent feature is prominent when comparing the calculations (red and green) and measurement (black) in Figs. 7 and 8 (and Figs. 10 and 11). The measurements show a significantly lower amount of light in the wavelength region above 2.7 μm (between 2.7 and 3.5 μm in Figs. 10 and 11), than what is found in simulations. As already mentioned in Subsection 4.B, we explain this by an attenuation band caused by water absorbed in the fiber. The band is qualitatively marked with vertical black solid lines in figures presenting spectra. The loss band provides a barrier that halts the SSFS, and consequently simulations with no artificial loss predict a longer wavelength edge than the measurement does. This is verified by the blue curve in Fig. 8(a), where the artificial loss is included in the simulation. The SC spectrum predicted by calculations that include the artificial loss show a behavior more similar to that of the measured SC spectrum. The overshoot by the simulation is now reduced, and also the short wavelength edge has better correspondence with the measured edge. GV matching the overshoot observed in the green and red curve of Figs. 7 and 8 on the long wavelength edge causes a similar overshoot of the short wavelength edge, and the spectrum is predicted to be too wide in either end. With the given data, we have obtained good agreement between the measured and predicted SC spectral development.

From Figs. 7 and 8 we can measure the width of the SC spectral output, with a limit of PSD(λ) > 1 nW/nm. The bandwidths become $\Delta\lambda^m = 2.05$ μm, $\Delta\lambda^c = 2.19$ μm, and $\Delta\lambda^c_{WS} = 2.33$ μm for the measured, calculated and wavelength-shifted calculated PSD, respectively, for pumping with $P_0 = 710$ kW. Increasing the power to $P_0 = 1180$ kW, we get $\Delta\lambda^m = 2.40$ μm, $\Delta\lambda^c = 2.52$ μm, and $\Delta\lambda^c_{WS} = 2.61$ μm, respectively. The deviation between measured and calculated SC spectral widths is less than 15% in the worst case. We see that the effect of wavelength-shifting the dispersion profile to shorter wavelengths is to shift the edge of the PSD similarly. It is also observed that the SC from the wavelength-shifted dispersion operator is the broadest. This is because the ZDW is moved closer to the pump, and consequently light is pushed into the anomalous dispersion regime at an earlier stage of propagation and soliton dynamics start sooner.

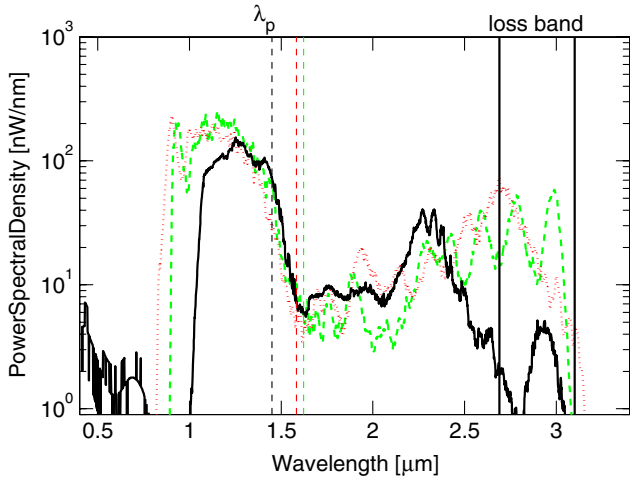

Fig. 7. (Color online) Measurement (black) and simulations (dashed green) of SCG for $\lambda_p = 1450$ nm and $P_0 = 710$ kW. The dotted red spectrum is obtained for the wavelength-shifted dispersion profile in Fig. [2]. Dashed vertical lines mark pump wavelength (black) and the ZDW (red, green) of the fiber.

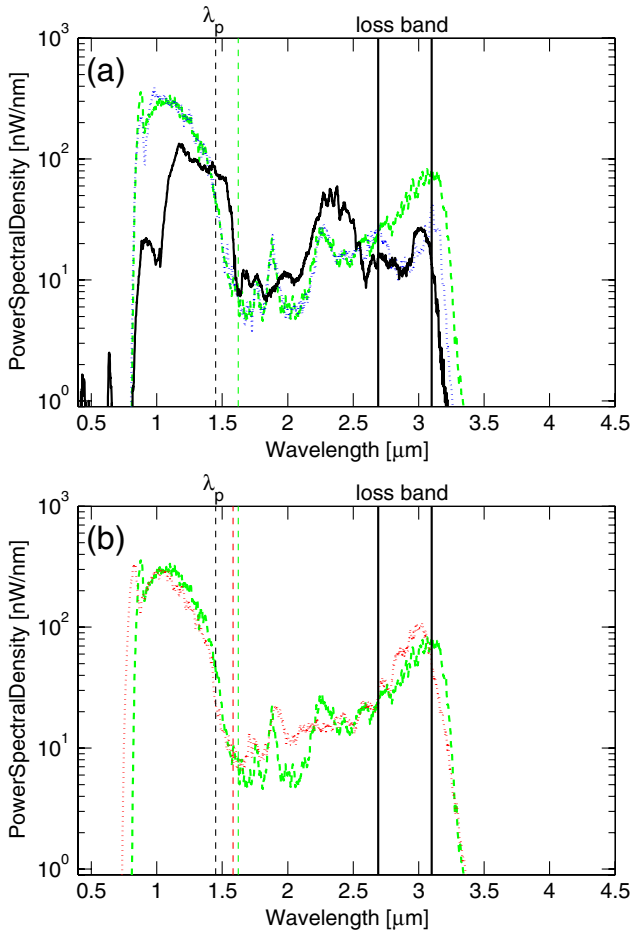

Fig. 8. (Color online) (a) Measurement (black) and simulations (dashed green) of SCG for $\lambda_p = 1450$ nm and $P_0 = 1180$ kW. The dotted blue curve shows the simulation with artificial loss shown in Fig. 3. (b) The dotted red spectrum is obtained for the wavelength-shifted dispersion profile shown in Fig. 2. Dashed vertical lines mark the pump wavelength (black) and the ZDW (red, green) of the fiber.

B. Anomalous Dispersion Regime Pumping

For pumping in the anomalous dispersion regime, the seed laser is set to $\lambda_p = 2000$ nm and $T_{\mathrm{FWHM}} = 110$ fs pulses. These parameters are fixed throughout our measurements and simulations in the anomalous dispersion regime.

In this anomalous pumping regime, the spectral development is entirely governed by soliton related dynamics, and the initial and final spectral development is illustrated in the spectrograms in Figs. 9(a)–9(c). The soliton fission process induced by higher order dispersion is well described in [45]. Initially, SPM and FWM broadens the pulse, before higher order dispersion causes fission of the higher order soliton excited in the fiber by the pump. The soliton number is $N \approx 14$ when pumping with $P_0 = 1110$ kW, but some amount of energy is clearly lost in the fission process. Correspondingly, we see the generation of only 6–7 solitons. After soliton fission, the individual solitons redshift by the SSFS and emit

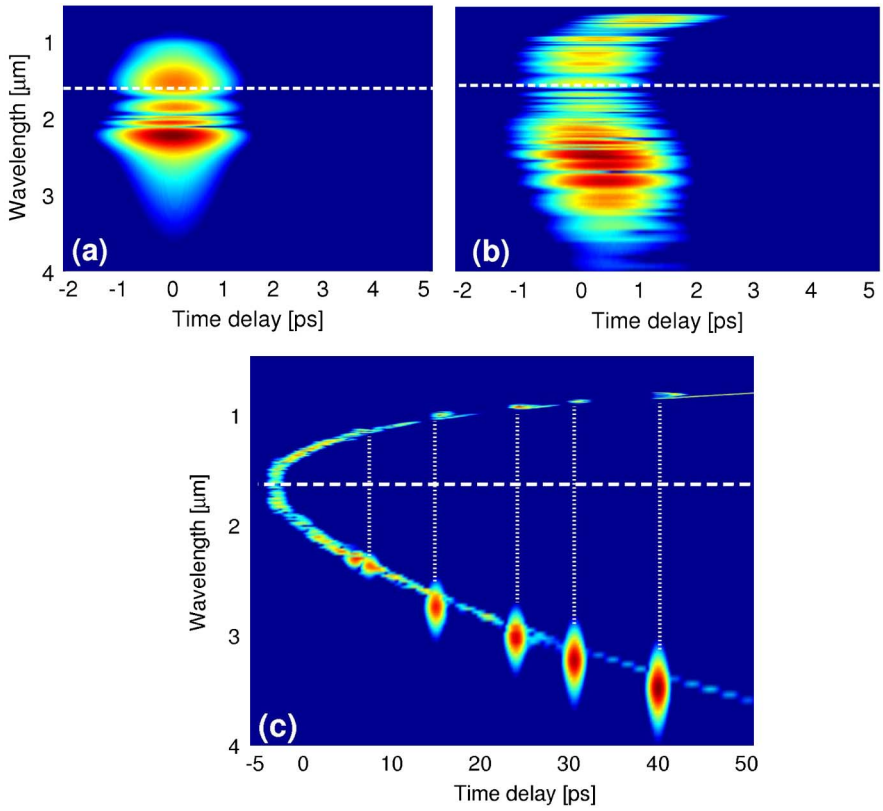

Fig. 9. (Color online) Spectrograms of the $\lambda_p = 2000$ nm and $P_0 = 1110$ kW simulation at (a) $z = 1.0$ cm, (b) $z = 5.3$ cm, and (c) $z = L$. White dashed lines mark the calculated ZDW of the fiber.

phase-matched dispersive waves at wavelengths shorter than the ZDW.

A comparison between measurement (black) and simulations (green) is shown in Figs. 10(a) and 10(b) for a peak power of $P_0 = 1110$ kW and in Fig. 11 for $P_0 = 2130$ kW. The red curve is calculated using the wavelength-shifted dispersion profile (dashed black in Fig. 2). The same trend as in Figs. 7 and 8 is observed in Figs. 10 and 11, where the level of measured PSD in the region from 2.7 to 3.5 μm is lower than the simulated level. However, the SSFS is so strong when pumping directly in the anomalous dispersion regime with such high peak powers that solitons can cross the loss band and shift to wavelengths longer than 3.5 μm. The long-wavelength edge is now ultimately determined by the fiber transmission window that stops around 4.5 μm. In Fig. 10(a), simulation including the artificial loss is shown in blue. The simulation confirms the trend that an attenuation is present in the experiment from around 2.7 μm, which is not accounted for by simulations without the artificially enhanced loss. However, the attenuation we introduced is not enough to exactly predict the location of the long-wavelength edge of the SC. This could be attributed to an uncertainty in the level of power coupled into the fiber. The location of the long-wavelength edge is sensitive to the peak power coupled into the fiber when pumping in the anomalous dispersion regime, and the value is based on an assessment. Another explanation could be the relatively low Raman gain.

From Figs. 10 and 11, we can find the bandwidth of the measured and the calculated SC spectra. The bandwidths become $\Delta\lambda^m = 3.0$ μm, $\Delta\lambda^c = 3.0$ μm, and $\Delta\lambda^c_{WS} = 3.1$ μm for low power $P_0 = 1110$ kW and $\Delta\lambda^m = 3.7$ μm, $\Delta\lambda^c = 3.6$ μm and $\Delta\lambda^c_{WS} = 3.6$ μm for high power $P_0 = 2130$ kW. The deviation between the measured and calculated SC spectral widths is in this regime less than 5%. In the anomalous pumping regime, we also see a small shifting of the entire spectrum to shorter wavelengths, when applying the wavelength-shifted dispersion profile.

6. DISCUSSION

There are several factors that can cause the discrepancies between the measured and calculated width of the generated SC, which we observe. The discrepancies can first and foremost be related to uncertainty in the fiber attenuation and dispersion (already discussed), as well as in the fiber core and the assessment of the peak power coupled into the fiber. Regarding the many different measurements of the Raman gain profile, we note that the main effect of a larger f_R value would be to redshift the long wavelength edge of the SC.

The assessment of the power coupled into the fiber is based on an autocorrelation of the input pulse along with measurements of the average power in the beam before and after propagation through the fiber. This is an indirect way of estimating the input power, which can cause disagreement between measured and calculated SC spectral widths. However, we are still able to predict the SC spectral width within 15% for normal dispersion regime pumping and within 5% for anomalous dispersion regime pumping.

However, to check the influence of the input peak power, we have in Fig. 12 repeated all calculations from Figs. 7–8 and 10–11, but with the peak power reduced by 20%. As expected,

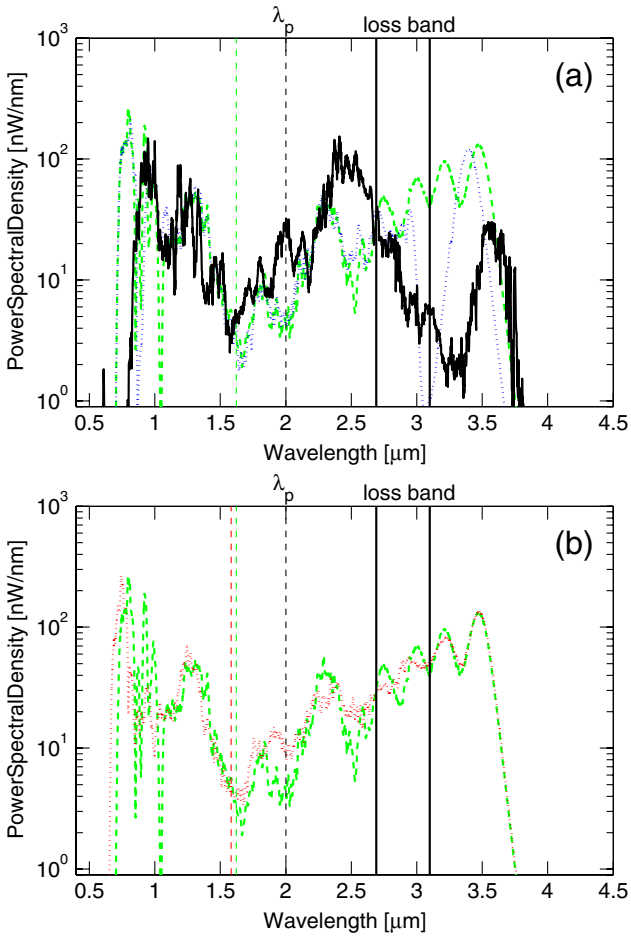

Fig. 10. (Color online) (a) Measurement (black) and simulations (dashed green and dotted blue) of the SCG for $\lambda_p = 2000$ nm and $P_0 = 1110$ kW. The dotted blue curve shows a simulation with the artificial loss shown in Fig. 3. (b) The dotted red spectrum is obtained for the wavelength-shifted dispersion profile shown in Fig. 2. Dashed vertical lines mark the pump wavelength (black) and the ZDW (red, green) of the fiber.

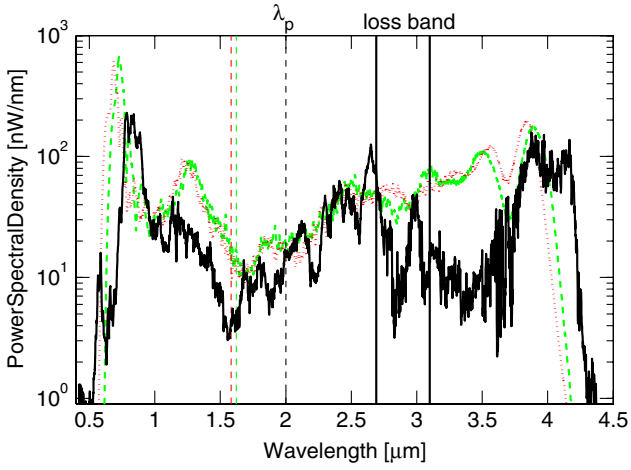

Fig. 11. (Color online) Measurement (black) and simulations (dashed green) of the SCG for $\lambda_p = 2000$ nm and $P_0 = 2130$ kW. The dotted red spectrum is obtained for the wavelength-shifted dispersion profile in Fig. 2. Dashed vertical lines mark the pump wavelength (black) and the ZDW (red, green) of the fiber.

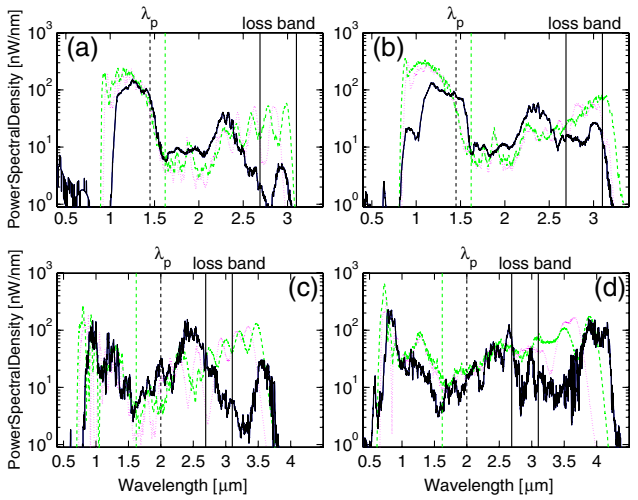

Fig. 12. (Color online) Measurements (black) and simulations (dashed green) of SCG. Top, normal pumping with $\lambda_p = 1450$ nm, $T_{\mathrm{FWHM}} = 145$ fs, and (a) $P_0 = 710$ kW and (b) $P_0 = 1180$ kW. Bottom, anomalous pumping with $\lambda_p = 2000$ nm, $T_{\mathrm{FWHM}} = 110$ fs, and (c) $P_0 = 1110$ kW and (d) $P_0 = 2130$ kW. Dashed magenta curves shows SCG for P_0 reduced by 20%.

all simulations show that both the long- and short-wavelength edges move toward the pump, thereby narrowing the bandwidth of the SC. For anomalous pumping [Figs. 12(c), 12(d)], the long-wavelength edge is now further away from the measured edge, which indicates that the first assessment of P_0 was closer to the actual value. For normal pumping at high power [Fig. 12(b)], the reduced power makes the numerical and experimental long wavelength edge coincide, whereas at low power it reduce the long wavelength edge to be below the experimental value. Generally we can conclude that the estimated peak power has not been too low. The fact that the lower peak power improves the correspondence in Fig. 12(b) underlines the fact that the accuracy of the estimated P_0 may differ from experiment to experiment, in particular when using free-space coupling.

7. CONCLUSION

We have presented a thorough investigation of the material parameters enabling reliable numerical modeling of SCG in a commercial ZBLAN optical fiber. We have presented measurements both on modal dispersion and Raman gain. Simulation and measurement show good agreement in both pumping regimes, and discrepancies are attributed primarily to an unknown attenuation in the experimental setup, which we conclude is caused by water absorption in the fiber, along with exact assessment of the pulse coupled into the fiber.

ACKNOWLEDGMENTS

The authors acknowledge support from the Danish National Advanced Technology Foundation. We are thankful for the cooperation of Masayoshi Horita, FiberLabs, Inc. We also wish to thank Kent Erik Mattsson for fruitful discussions about the absorption spectra in ZBLAN and Karsten Rottwitt for discussions about the Raman effect in optical fibers.

REFERENCES

1. R. R. Alfano and S. L. Shapiro, "Emission in the region 4000 to 7000 Å via four-photon coupling in glass," Phys. Rev. Lett. **24**, 584–587 (1970).
2. E. R. Andresen, C. K. Nielsen, J. Thøgersen, and S. R. Keiding, "Fiber laser-based light source for coherent anti-Stokes Raman scattering microspectroscopy," Opt. Express **15**, 4848–4856 (2007).
3. A. Aguirre, N. Nishizawa, J. Fujimoto, W. Seitz, M. Lederer, and D. Kopf, "Continuum generation in a novel photonic crystal fiber for ultrahigh resolution optical coherence tomography at 800 nm and 1300 nm," Opt. Express **14**, 1145–1160 (2006).
4. J. M. Dudley, G. Genty, and S. Coen, "Supercontinuum generation in photonic crystal fiber," Rev. Mod. Phys. **78**, 1135–1184 (2006).
5. N. Savage, "Supercontinuum sources," Nat. Photon. **3**, 114–115 (2009).
6. T. M. Monro and H. Ebendorff-Heidepriem, "Progress in microstructured optical fibers," Ann. Rev. Mater. Res. **36**, 467–495 (2006).
7. C. Xia, M. Kumar, O. P. Kulkarni, M. N. Islam, J. Fred, L. Terry, M. J. Freeman, M. Poulain, and G. Maze, "Mid-infrared supercontinuum generation to 4.5 μm in ZBLAN fluoride fibers by nanosecond diode pumping," Opt. Lett. **31**, 2553–2555 (2006).
8. G. Qin, X. Yan, C. Kito, M. Liao, C. Chaudhari, T. Suzuki, and Y. Ohishi, "Ultrabroadband supercontinuum generation from ultraviolet to 6.28 μm in a fluoride fiber," Appl. Phys. Lett. **95**, 161103 (2009).
9. L. Liu, G. Qin, Q. Tian, D. Zhao, and W. Qin, "Numerical investigation of mid-infrared supercontinuum generation up to 5 μm in single mode fluoride fiber," Opt. Express **19**, 10041–10048 (2011).
10. Z. Chen, A. J. Taylor, and A. Efimov, "Coherent mid-infrared broadband continuum generation in non-uniform ZBLAN fiber taper," Opt. Express **17**, 5852–5860 (2009).
11. W. Q. Zhang, S. A. V., and T. M. Monro, "A genetic algorithm based approach to fiber design for high coherence and large bandwidth supercontinuum generation," Opt. Express **17**, 19311–19327 (2009).
12. R. E. Slusher, G. Lenz, J. Hodelin, J. Sanghera, L. B. Shaw, and I. D. Aggarwal, "Large Raman gain and nonlinear phase shifts in high-purity As_2Se_3 chalcogenide fibers," J. Opt. Soc. Am. B **21**, 1146–1155 (2004).
13. R. T. White and T. M. Monro, "Cascaded Raman shifting of high-peak-power nanosecond pulses in As_2S_3 and As_2Se_3 optical fibers," Opt. Lett. **36**, 2351–2353 (2011).
14. D. D. Hudson, S. A. Dekker, E. C. Mägi, A. C. Judge, S. D. Jackson, E. Li, J. S. Sanghera, L. B. Shaw, I. D. Aggarwal, and B. J. Eggleton, "Octave spanning supercontinuum in an As_2Se_3 taper using ultralow pump pulse energy," Opt. Lett. **36**, 1122–1124 (2011).
15. S. D. Le, D. M. Nguyen, M. Thual, L. Bramerie, M. C. e Silva, K. Lengle, M. Gay, T. Chartier, L. Brilland, D. Méchin, P. Toupin, and J. Troles, "Efficient four-wave mixing in an ultra-highly nonlinear suspended-core chalcogenide $As_{38}Se_{62}$ fiber," Opt. Express **19**, B653–B660 (2011).
16. M. Liao, X. Yan, G. Qin, C. Chaudhari, T. Suzuki, and Y. Ohishi, "A highly non-linear tellurite microstructure fiber with multi-ring holes for supercontinuum generation," Opt. Express **17**, 15481–15490 (2009).
17. S. Dupont, C. Petersen, J. Thøgersen, C. Agger, O. Bang, and S. R. Keiding, "IR microscopy utilizing intense supercontinuum light source," Opt. Express **20**, 4887–4892 (2012).
18. C. L. Hagen, J. W. Walewski, and S. T. Sanders, "Generation of a continuum extending to the midinfrared by pumping ZBLAN fiber with an ultrafast 1550 nm source," IEEE Photon. Technol. Lett. **18**, 91–93 (2006).
19. C. Xia, Z. Xu, M. Islam, F. Terry, M. Freeman, A. Zakel, and J. Mauricio, "10.5 W time-averaged power mid-ir supercontinuum generation extending beyond 4 μm with direct pulse pattern modulation," IEEE J. Sel. Top. Quantum Electron. **15**, 422–434 (2009).
20. D. Anderson, M. Lisak, B. Malomed, and M. Quiroga-Teixeiro, "Tunneling of an optical soliton through a fiber junction," J. Opt. Soc. Am. B **11**, 2380–2384 (1994).
21. C. Agger, S. T. Sørensen, C. L. Thomsen, S. R. Keiding, and O. Bang, "Nonlinear soliton matching between optical fibers," Opt. Lett. **36**, 2596–2598 (2011).
22. C. Petersen, S. Dupont, C. Agger, J. Thøgersen, O. Bang, and S. R. Keiding, "Stimulated Raman scattering in soft glass fluoride fibers," J. Opt. Soc. Am. B **28**, 2310–2313 (2011).
23. X. Yan, C. Kito, S. Miyoshi, M. Liao, T. Suzuki, and Y. Ohishi, "Raman transient response and enhanced soliton self-frequency shift in ZBLAN fiber," J. Opt. Soc. Am. B **29**, 238–243 (2011).
24. D. Buccoliero, H. Steffensen, O. Bang, H. Ebendorff-Heidepriem, and T. M. Monro, "Thulium pumped high power supercontinuum in loss-determined optimum lengths of tellurite photonic crystal fiber," Appl. Phys. Lett. **97**, 061106 (2010).
25. M. H. Frosz, "Validation of input-noise model for simulations of supercontinuum generation and rogue waves," Opt. Express **18**, 14778–14787 (2010).
26. J. Lægsgaard, "Mode profile dispersion in the generalised nonlinear Schrödinger equation," Opt. Express **15**, 16110–16123 (2007).
27. J. Hult, "A fourth-order Runge–Kutta in the interaction picture method for simulating supercontinuum generation in optical fibers," J. Lightwave Technol. **25**, 3770–3775 (2007).
28. A. M. Heidt, "Efficient adaptive step size method for the simulation of supercontinuum generation in optical fibers," J. Lightwave Technol. **27**, 3984–3991 (2009).
29. O. V. Sinkin, R. Holzlöhner, J. Zweck, and C. R. Menyuk, "Optimization of the split-step Fourier method in modeling optical-fiber communications systems," J. Lightwave Technol. **21**, 61–68 (2003).
30. K. Blow and D. Wood, "Theoretical description of transient stimulated Raman scattering in optical fibers," IEEE J. Quantum Electron. **25**, 2665–2673 (1989).
31. M. Horita, FiberLabs, KDDI Laboratories Building, 2-1-15 Ohara, Fujimino-shi, Saitama 356-8502, Japan (private communication, 2011).
32. S. T. Sørensen, A. Judge, C. L. Thomsen, and O. Bang, "Optimum fiber tapers for increasing the power in the blue edge of a supercontinuum—group-acceleration matching," Opt. Lett. **36**, 816–818 (2011).
33. M. Frosz, P. Falk, and O. Bang, "The role of the second zero-dispersion wavelength in generation of supercontinua and bright-bright soliton-pairs across the zero-dispersion wavelength," Opt. Express **13**, 6181–6192 (2005).
34. F. Gan, "Optical properties of fluoride glasses: a review," J. Non-Cryst. Solids **184**, 9–20 (1995).
35. J. Y. Lee and D. Y. Kim, "Versatile chromatic dispersion measurement of a single mode fiber using spectral white light interferometry," Opt. Express **14**, 11608–11615 (2006).
36. S. R. Loehr and C. T. Moynihan, "Effect of H_2O partial pressure on the rate of hydration of ZrF_4—BaF_2—LaF_3—AlF_3 glass," Mater. Sci. Forum **32–33**, 261–265 (1991).
37. D. Szebesta, S. Davey, J. Williams, and M. Moore, "OH absorption in the low loss window of ZBLAN(P) glass fibre," J. Non-Cryst. Solids **161**, 18–22 (1993).
38. G. Agrawal, *Nonlinear Fiber Optics*, 4th ed. (Academic, 2006).
39. R. H. Stolen, J. P. Gordon, W. J. Tomlinson, and H. A. Haus, "Raman response function of silica-core fibers," J. Opt. Soc. Am. B **6**, 1159–1166 (1989).
40. R. M. Almeida and J. D. Mackenzie, "Vibrational spectra and structure of fluorozirconate glasses," J. Chem. Phys. **74**, 5954–5961 (1981).
41. Y. Durteste, M. Monerie, and P. Lamouler, "Raman amplification in fluoride glass fibres," Electron. Lett. **21**, 723–724 (1985).
42. T. Mizunami, H. Iwashita, and K. Takagi, "Gain saturation characteristics of Raman amplification in silica and fluoride glass optical fibers," Opt. Commun. **97**, 74–78 (1993).
43. A. Saïssy, J. Botineau, L. Macon, and G. Maze, "Diffusion Raman dans une fibre optique en verre fluoré," J. Phys. Lett. **46**, 289–294 (1985).
44. T. Nakai, N. Norimatsu, Y. Noda, O. Shinbori, and Y. Mimura, "Changes in refractive index of fluoride glass fibers during fiber fabrication processes," Appl. Phys. Lett. **56**, 203–205 (1990).

45. A. V. Husakou and J. Herrmann, "Supercontinuum generation, four-wave mixing, and fission of higher-order solitons in photonic-crystal fibers," J. Opt. Soc. Am. B **19**, 2171–2182 (2002).
46. C. Lin, V. Nguyen, and W. French, "Wideband near-i.r. continuum (0.7 – 2.1 μm) generated in low-loss optical fibres," Electron. Lett. **14**, 822–823 (1978).
47. P. Beaud, W. Hodel, B. Zysset, and H. Weber, "Ultrashort pulse propagation, pulse breakup, and fundamental soliton formation in a single-mode optical fiber," IEEE J. Quantum Electron. **23**, 1938–1946 (1987).
48. J. M. Stone and J. C. Knight, "Visibly 'white' light generation in uniform photonic crystal fiber using a microchip laser," Opt. Express **16**, 2670–2675 (2008).